



Zn doping modulation of carrier transport properties at the back interface of antimony sulfide solar cells

Ying-Sen Xia¹, Jun-Cai Zhang¹, Jie Huang¹, Jin-Rui Cai¹, Ling-Jie Liu¹, Gan Huang¹, Li-Mei Lin^{1,*}, Zhi-Ping Huang¹, Hu Li^{1,*}, Shuiyuan Chen^{1,2,*}, Gui-Lin Chen^{1,2,*}

Keywords:

Sb₂S₃ solar cells, Zn doping, interface engineering, carrier transport

Citation:

Xia, Y. S.; Zhang, J. C.; Huang, J.; Cai, J. R.; Liu, L. J.; Huang, G.; Lin, L. M.; Huang, Z. P.; Li, H.; Chen, S.; Chen, G. L. Zn doping modulation of carrier transport properties at the back interface of antimony sulfide solar cells. *Energy Mater.* 2026, 6, 600022. <https://dx.doi.org/10.20517/energymater.2025.225>

Received: 24 Dec 2025

Accepted: 29 Jan 2026

Published: 16 Mar 2026

Academic Editor:

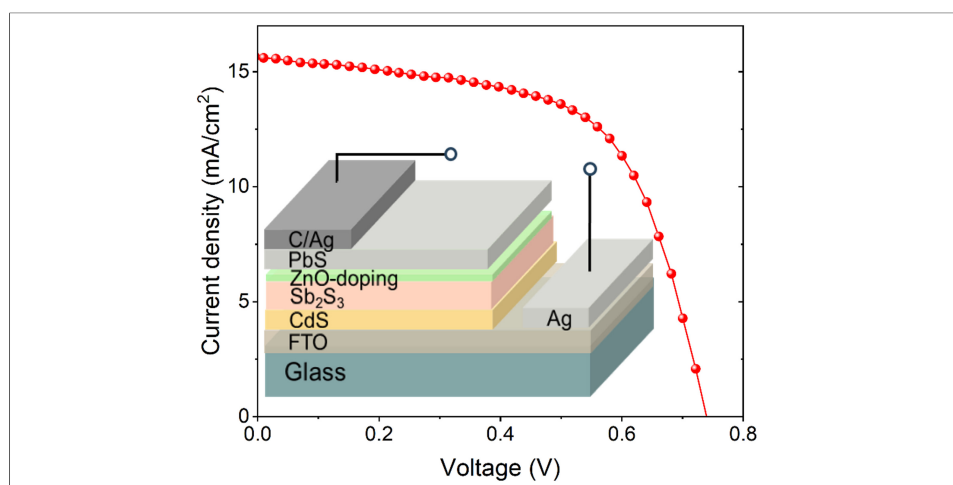
Soo Young Kim

Copy Editor:

Ping Zhang

Production Editor:

Ping Zhang



Abstract

Sb₂S₃ has emerged as a highly promising material for thin-film solar cells due to its low toxicity, excellent stability, and strong light absorption in the visible region. However, challenges such as the formation of the Sb₂O₃ secondary phase and S re-evaporation still exist during the high-temperature annealing of Sb₂S₃. To address these issues, this study introduces a strategy involving the pre-deposition of an ultrathin ZnO protective layer onto the Sb₂S₃ surface. The ZnO layer facilitates controlled oxygen passivation through a lattice-vacancy-mediated mass transfer mechanism, effectively suppressing the formation of Sb₂O₃ and minimizing Sb₂S₃ volatilization, while simultaneously forming a Zn-doping layer. The results show that Zn doping significantly enhances the energy level alignment at the back interface: the conduction band minimum (CBM) and valence band maximum (VBM) of the Sb₂O₃/Sb₂S₃ mixed layer are upshifted, and the Fermi level is downshifted, thereby promoting hole transport. Additionally, the carrier concentration increases,



¹Fujian Provincial Engineering Technology Research Center of Solar Energy Conversion and Energy Storage, College of Physics and Energy, Fujian Normal University, Fuzhou 350117, Fujian, China.

²Fujian Provincial Collaborative Innovation Center for Advanced High-Field Superconducting Materials and Engineering, Fuzhou 350117, Fujian, China.

*Correspondence to: Dr. Li-Mei Lin, Dr. Hu Li, Fujian Provincial Engineering Technology Research Center of Solar Energy Conversion and Energy Storage, College of Physics and Energy, Fujian Normal University, Fuzhou 350117, Fujian, China. E-mail: linlm@fjnu.edu.cn; lihu2025@163.com; Prof. Gui-Lin Chen, Prof. Shuiyuan Chen, Fujian Provincial Engineering Technology Research Center of Solar Energy Conversion and Energy Storage, College of Physics and Energy, Fujian Normal University, Fuzhou 350117, Fujian, China; Fujian Provincial Collaborative Innovation Center for Advanced High-Field Superconducting Materials and Engineering, Fuzhou 350117, Fujian, China. E-mail: glchen@fjnu.edu.cn; sychen@fjnu.edu.cn

reducing the contact barrier with the carbon electrode. This modification enables the power conversion efficiency (PCE) of all-inorganic Sb_2S_3 solar cells with fluorine-doped tin oxide (FTO)/ $\text{CdS}/\text{Sb}_2\text{S}_3/\text{PbS}/\text{Carbon}/\text{Ag}$ structures to reach an impressive 7.00%, representing the most advanced performance level currently available and providing new guidance for the development of high-performance and low-cost all-inorganic Sb_2S_3 solar cells.

INTRODUCTION

In recent years, antimony-based solar cells have achieved rapid development due to their environmentally friendly characteristics and excellent physical properties^[1,2]. Among them, antimony sulfide (Sb_2S_3) has gained significant attention as a promising light-absorbing material for thin-film solar cells, thanks to its near-ideal bandgap of 1.7 eV, high visible-light absorption coefficient ($> 5 \times 10^4 \text{ cm}^{-1}$), low toxicity, and excellent environmental stability^[3,4]. Since Savadogo's pioneering work on chemically deposited Sb_2S_3 films and photoelectrochemical cells in 1992^[5], substantial progress has been made^[6,7]. Solution-based techniques, particularly chemical bath deposition (CBD) and hydrothermal synthesis, have dominated due to their low equipment requirements and scalability. Notably, in 2025, Shen *et al.* achieved a record-breaking 8.26% power conversion efficiency (PCE) by developing ethylenediaminetetraacetic acid disodium salt as an additive to regulate the reaction kinetics for Sb_2S_3 deposition^[8]. However, these efficiencies remain significantly below the Shockley-Queisser (S-Q) limit (28.6%)^[9]. The S-Q analysis predicts maximum values of open-circuit voltage (V_{oc}) = 1.402 V, short circuit current density (J_{sc}) = 22.5 mA/cm^2 , and fill factor (FF) = 91%. In contrast, state-of-the-art devices (e.g., 8.26% PCE) exhibit substantially lower parameters: V_{oc} = 0.707 V (50.4% of limit), J_{sc} = 17.91 mA/cm^2 (79.6%), and FF = 64.81% (71.2%)^[8]. The severe deficit in V_{oc} is particularly critical, attributed primarily to interfacial recombination, inefficient carrier collection, and intrinsic material defects. Among them, suppressing interface recombination to enhance the extraction efficiency of electrons and holes has become an effective way to improve device performance.

Annealing, as a crucial step after the deposition of Sb_2S_3 thin films, should be carried out at 300–450 °C, which drives the transformation of the amorphous phase to the crystalline phase through thermal rearrangement and simultaneously enhances the ion diffusion rate^[10]. However, this process faces multiple challenges: Firstly, the essential annealing at high temperatures, aggravating the re-evaporation of sulfur and Sb_2S_3 due to their high saturated vapor pressure, leads to surface defects, film non-uniformity, and even exposure of the underlying CdS layer, which finally disrupts the integrity of the p-n junction. Secondly, residual oxygen reacting with antimony forms harmful Sb_2O_3 secondary phases at high temperature, which not only disrupts interface flatness and continuity but also introduces carrier recombination centers, significantly reducing device efficiency^[11]. Thirdly, the re-crystallization of Sb_2S_3 delivers a low-level position of valence band energy which creates severe band mismatch with the back electrode. To address the above challenges, researchers have explored the introduction of stable metal oxide buffer layers at the back interface during annealing. For instance, a Ni/Ti co-doped MoO_3 hole transport layer (HTL) can effectively extract holes from the metal halide perovskite layer, achieving a PCE of 18.1% in perovskite solar cells^[12]. When WO_{3-x} is used as the HTL, the formation of Sb-W bonds at the $\text{Sb}_2\text{S}_3/\text{WO}_{3-x}$ interface creates an interface dipole, which not only reduces the hole extraction barrier but also effectively suppresses back interface recombination in Sb_2S_3 devices^[13]. Additionally, first-principles calculations by Professor Chen's team demonstrated that Zn doping in Sb_2S_3 can lower the Fermi level and increase the conductivity^[14,15]. And Tang *et al.* further confirmed that solution-processed Zn doping can elevate the back surface energy level of Sb_2S_3 , improve carrier transport, and reduce interface recombination^[16]. These strategies based on oxide buffer layers or metal element doping all provide effective ways to improve the photovoltaic performance of Sb_2S_3 .

Building on interface engineering and doping strategies, this work employs an ultrathin ZnO layer as an oxygen diffusion barrier, referred to as a “breathing membrane”. This layer enables controlled oxygen

passivation of the underlying Sb_2S_3 film via a lattice-vacancy-mediated mass transfer mechanism, effectively inhibiting the formation of Sb_2O_3 and reducing interface defects, *etc.* Critically, the selection of ZnO also considers potential Zn^{2+} substitutional doping at the Sb_2S_3 /oxide interface, which modulates interfacial energy levels and enhances carrier concentration. This synergistic approach concurrently optimizes the phase composition, morphology, and electrical properties of the Sb_2S_3 back surface, thereby improving carrier transport efficiency. Ultimately, a PCE of 7.00% was achieved in a fully inorganic fluorine-doped tin oxide (FTO)/CdS/ Sb_2S_3 /PbS/Carbon/Ag architecture, offering a novel route toward more efficient and stable Sb_2S_3 solar cells.

EXPERIMENTAL

Chemicals

Cadmium nitrate tetrahydrate [$\text{Cd}(\text{NO}_3)_2 \cdot 4\text{H}_2\text{O}$], ammonium hydroxide ($\text{NH}_3 \cdot \text{H}_2\text{O}$), thiourea ($\text{CH}_4\text{N}_2\text{S}$), and cadmium chloride hemipentahydrate ($\text{CdCl}_2 \cdot 2.5\text{H}_2\text{O}$) were purchased from Sinopharm Chemical Reagent Co., Ltd. (Shanghai, China). Methanol (CH_3OH), potassium antimony tartrate hemihydrate ($\text{C}_4\text{H}_4\text{KO}_7\text{Sb} \cdot 0.5\text{H}_2\text{O}$), and lead acetate trihydrate ($\text{PbC}_4\text{H}_6\text{O}_4 \cdot 3\text{H}_2\text{O}$) were supplied by Shanghai Macklin Biochemical Co., Ltd. (Shanghai, China). Zinc oxide (ZnO), and sodium thiosulfate pentahydrate ($\text{Na}_2\text{S}_2\text{O}_3 \cdot 5\text{H}_2\text{O}$) were supplied by Aladdin Reagent Co., Ltd. (Shanghai, China). The carbon ink (C, CH-8) was supplied by Jujo printing supplies & Technology Co. Ltd. (Zhejiang, China). The silver conductive paint (Ag, 05002-AB) was supplied by Structure Probe, Inc (USA). All the chemicals were used as received without further purification.

CdS electron transport layer preparation

Commercial FTO was ultrasonically cleaned with detergent, acetone, anhydrous ethanol, and ultrapure water sequentially for 60 min, dried, and ozone-treated for 20 min to remove surface organics/impurities. The FTO substrate with the conductive surface facing down was placed into a 100 mL deionized water solution containing 0.15 mM cadmium nitrate tetrahydrate, 9.4 mM thiourea and 0.19 mol ammonium hydroxide. The mixed solution was then placed in a 65 °C water bath for 15 min to deposit the CdS film. To improve the crystallinity, 0.05 g $\text{CdCl}_2 \cdot 2.5\text{H}_2\text{O}$ dissolved in 10 mL methanol was spin-coated on CdS, annealed in air at 380 °C for 5 min, then cooled naturally.

Sb_2S_3 and ZnO preparation

Dissolve 0.12 mol of sodium thiosulfate pentahydrate as the sulfur source and 0.06 mol of potassium antimony tartrate hemihydrate as the antimony source in 40 mL of deionized water respectively, then mix them to form 80 mL of solution. The mixture and three FTO/CdS substrates were transferred into a 100 mL Teflon-lined autoclave vessel. Seal the autoclave and heat it at 120 °C for 12 h. After the hydrothermal reaction, wash the sample with deionized water and then dry it under normal pressure on a hot plate to obtain the Sb_2S_3 precursor film.

Prepare the ZnO protective layer by radio frequency magnetron sputtering. The specific process parameters are as follows: the sputtering base pressure is less than 1.0×10^{-3} Pa, the working gas is a mixture of argon and oxygen ($\text{Ar}:\text{O}_2 = 9:1$), the sputtering power is set at 60 W, and the sputtering time is controlled at 20–400 s. Then, place the sample in a closed space and perform annealing in an ambient air atmosphere in an inverted manner. The annealing temperature is 450 °C for 3 min. Nine devices were fabricated under each experimental condition to support statistical analysis.

HTL and Electrode fabrication

Deposit PbS by in-situ hydrothermal method. Dissolve 3.3 mM of lead acetate trihydrate ($\text{PbC}_4\text{H}_6\text{O}_4 \cdot 3\text{H}_2\text{O}$) and 17.4 mM of sodium thiosulfate pentahydrate ($\text{Na}_2\text{S}_2\text{O}_3 \cdot 5\text{H}_2\text{O}$) in 50 mL of deionized water to form a clear

solution. Immerse the Sb_2S_3 film in the above solution in a 100 mL Teflon-lined autoclave, seal it, and heat it at 120 °C for 35 min. Apply carbon ink on the HTL and bake it at 120 °C on a hot plate for 30 min. Apply silver paste on the carbon layer and bake it at 80 °C for 10 min to complete the device fabrication. The total fabrication time for a complete device is approximately 2 to 3 days. Finally, a total of 54 devices were fabricated to validate the statistical reliability of the results.

Characterization

In this work, we used a field emission scanning electron microscope (SU-8010; Hitachi High-Tech, Japan) equipped with energy dispersive X-ray (EDX) to characterize the surface and elemental composition of the selenated antimony original mineral films. The crystal structures of the surface and powder of the selenated antimony original mineral films were characterized by X-ray diffraction (Ultima IV; Rigaku Corporation, Japan). The transmittance of the thin film was measured by ultraviolet–visible spectroscopy (UV-Vis) absorption spectroscopy (Lambda 950; PerkinElmer, USA). The current density-voltage (J - V) curves were collected using a Keithley 2400 source meter (Keithley 2400; Keithley Instruments, USA) under simulated AM 1.5G by the solar simulator (Newport 94023A; Newport Corporation, USA). The external quantum efficiency (EQE) of the devices was performed by a solar cell quantum efficiency measurement system (QEX10; PV Measurements, Inc., USA). Carrier transport and recombination mechanisms were investigated through electrochemical impedance spectroscopy (EIS) and dark capacitance-voltage (C - V) analysis. The Raman measurement was performed using the LABRAM-HR microRaman system with a 532 nm laser light source (LabRAM HR Evolution; HORIBA Scientific, France).

RESULTS AND DISCUSSION

The surface morphology of Sb_2S_3 precursor films, with and without the ZnO modification layer, was first analyzed by scanning electron microscopy (SEM). As depicted in [Supplementary Figure 1](#), the deposition of an ultrathin ZnO layer did not significantly alter the initial morphology; both samples displayed characteristic large-grained structures formed from agglomerated nanocrystals, typical of hydrothermally grown Sb_2S_3 films. However, post-annealing morphological evolution revealed stark contrasts, as shown in [Figure 1](#). The unmodified sample (W/O ZnO) formed ~50 nm $\text{Sb}_2\text{O}_3/\text{Sb}_2\text{S}_3$ particles and ~40 nm Sb_2O_3 nanobelts at grain boundaries. By contrast, ZnO-coated films exhibited notable morphological refinements: the 20 s ZnO sample showed smaller particles (~30 nm) and narrower nanobelts (~20 nm), with coarsening observed at longer deposition times. This coarsening is attributed to ZnO-mediated suppression of Sb_2S_3 volatilization, which increases the local Sb_2S_3 availability for oxidation and promotes Sb_2O_3 growth supported by subsequent compositional analysis.

Cross-sectional SEM imaging (the inset of [Figure 1](#)) corroborated these findings. The control film (W/O ZnO) displayed a highly uneven thickness (~350 nm) due to extensive Sb_2S_3 loss during annealing, along with the presence of large Sb_2O_3 surface particles. Incorporation of a 20 s ZnO layer mitigated volatilization, resulting in a more uniform film with increased thickness (~500 nm). Extended ZnO deposition (≥ 40 s) further improved thickness (up to ~600 nm) and significantly reduced Sb_2O_3 surface features. Elemental analysis via energy-dispersive X-ray spectroscopy (EDS) quantified atomic percentages of Sb, S, O, and Zn [[Supplementary Figure 2A](#)]. Key trends include: (1) relatively stable Sb content, (2) a non-monotonic variation in S content, (3) an initial decrease followed by an increase in O content, and (4) a clear upward trend in Zn concentration (from ~0.1% to ~1.2 at.%). The elevated oxygen and decreased sulfur levels at 400 s ZnO are attributed to thick ZnO layers contributing additional oxygen. The increasing Zn/Sb atomic ratio [[Supplementary Figure 2B](#)] further confirms progressive Zn incorporation into the Sb_2S_3 matrix with extended ZnO exposure.

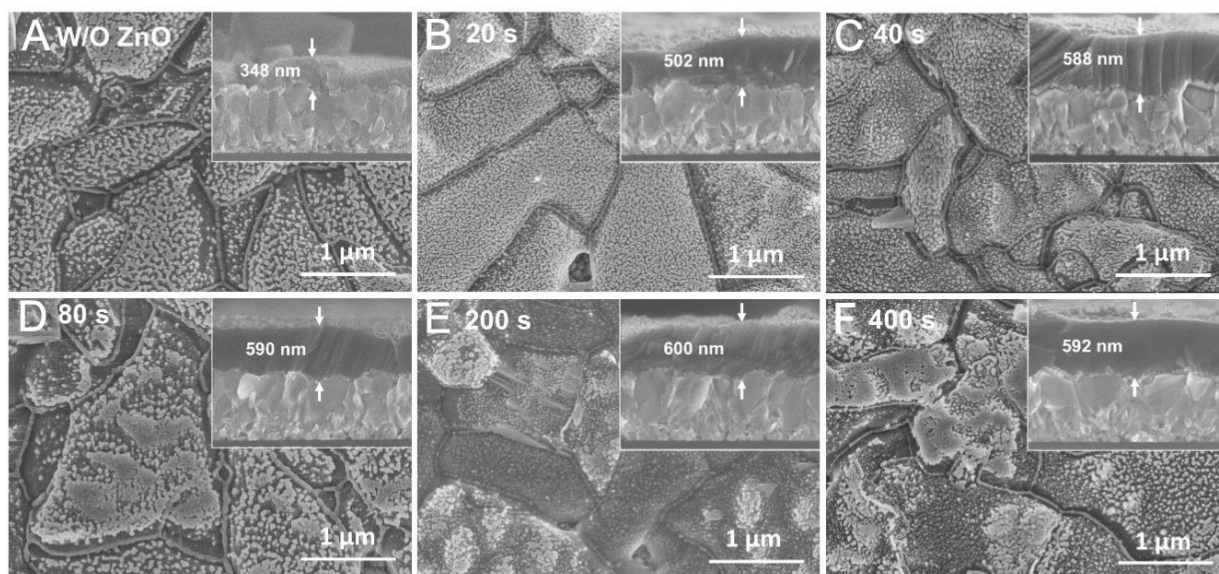


Figure 1. Surface and cross-sectional morphologies of Sb_2S_3 thin films (A) without ZnO and with ZnO deposited with (B) 20 s, (C) 40 s, (D) 80 s, (E) 200 s and (F) 400 s. SEM: Scanning electron microscope; W/O: without ZnO.

To evaluate the photovoltaic impact of ZnO incorporation, Sb_2S_3 solar cells were fabricated using a hydrothermally deposited PbS HTL, paste-coated carbon and Ag contacts. The statistical results of the average values of J - V measurements [Figure 2A and Table 1] show that the enhancement effect of the ZnO modified devices is consistent. The V_{oc} remained above 700 mV for all ZnO-treated samples, peaking at 40 s due to reduced Sb_2S_3 degradation and minimized leakage pathways. The optimal 40 s ZnO condition coincides with minimized resistive Sb_2O_3 formation and improved bulk conductivity, facilitating efficient carrier extraction. The J_{sc} increased by 17% at 40 s ZnO (14.6 mA/cm^2) compared to the control, then declined with thicker ZnO layers. Similarly, the FF reached an optimal average of 59% at 40 s, but dropped to ~50% at $\geq 80 \text{ s}$, consistent with increased series resistance and impeded hole transport from thicker ZnO layers. Consequently, the highest PCE of 7.00% was attained under 40 s ZnO conditions ($V_{oc} = 729 \text{ mV}$, $J_{sc} = 15.6 \text{ mA/cm}^2$, FF = 61.5%), representing a 20% improvement over the unmodified reference device. Although this device performance still lags behind that of Spiro-OMeTAD/metal electrodes and Sb_2S_3 -based tandem devices^[17,18], this study provides a practical strategy for the low-cost fabrication of solar cells employing all-inorganic carbon electrodes.

X-ray diffraction (XRD) analysis [Figure 2B] verified the crystallographic composition of annealed films, identifying orthorhombic Sb_2S_3 (PDF#42-1393) as the dominant phase, with minor peaks corresponding to cubic Sb_2O_3 (PDF#71-0365). Notably, the intensity of the Sb_2O_3 (222) peak at 27.68° decreased systematically with longer ZnO deposition [Supplementary Figure 3A and B], indicating suppressed secondary oxide formation. A weak ZnO (100) peak appeared only at 80 s ZnO, while no ZnO diffraction was detectable at shorter deposition times ($\leq 40 \text{ s}$), underscoring the ultrathin and amorphous nature of ZnO in those cases. These results confirm that the ZnO interlayer effectively retards Sb_2O_3 phase formation during air annealing.

To understand the origin of these enhancements, grazing-incidence XRD (GIXRD) at 2° incidence [Supplementary Figure 4] revealed no residual ZnO phase in the 40 s ZnO film post-annealing, suggesting Zn substitution within the Sb_2S_3 or Sb_2O_3 lattices. Detailed peak analysis [Figure 2C] showed systematic shifts of major Sb_2S_3 and Sb_2O_3 peaks toward higher angles, consistent with lattice contraction per Bragg's law ($d = \lambda/2\sin\theta$). When larger Zn^{2+} (134 pm) replaces Sb^{3+} (140 pm), the smaller ionic radius causes lattice contraction, which is the direct origin of the aforementioned peak shift. Further observation also reveals that

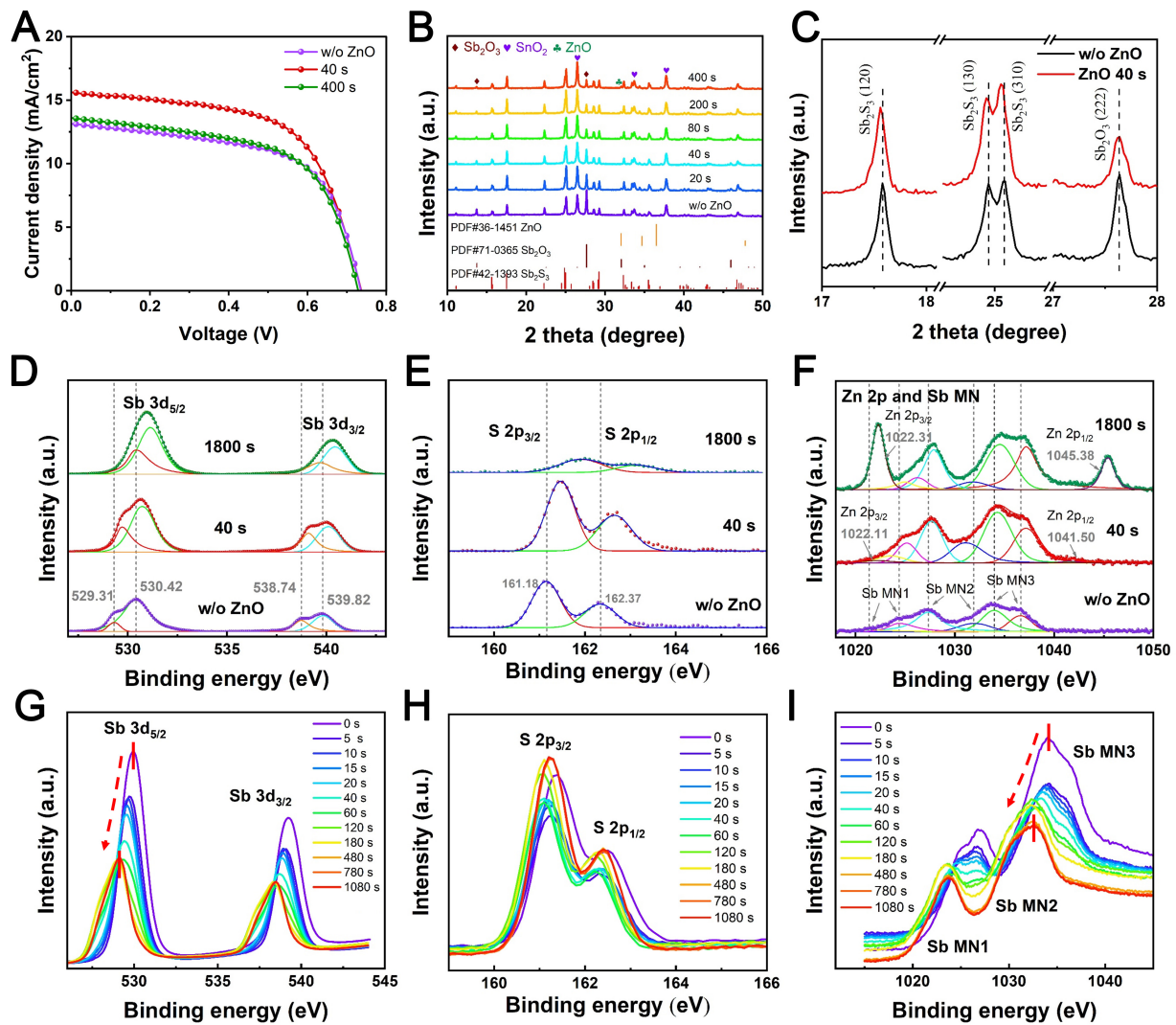


Figure 2. (A) *J*-*V* curves and (B) XRD patterns of Sb₂S₃ doped with ZnO with different deposition times; (C) The magnified XRD pattern of the Sb₂S₃ films; (D) Sb 3d, (E) S 2p and (F) Zn 2p XPS spectra of Sb₂S₃ thin films with and without ZnO. High-resolution (G) Sb 3d, (H) S 2p, (I) Sb MN XPS spectra. *J*-*V*: Density-voltage; XRD: X-ray diffraction; XPS: X-ray photoelectron spectroscopy; PDF: powder diffraction file; MN: X-ray photoelectron spectrum peak of Sb; W/O: without ZnO.

Table 1. The performance parameters list of Sb₂S₃ solar cells without and with ZnO

Sample	V_{oc} (mV)	J_{sc} (mA/cm ²)	R_s (Ω)	R_{sh} (kΩ)	FF (%)	PCE (%)
W/O ZnO	729.6	12.5 ± 1.2	158 ± 86	3.2 ± 0.4	56.6	5.1 ± 0.9
20 s	727.8	13.4 ± 0.7	143 ± 49	3.0 ± 0.2	58.4	5.4 ± 0.6
40 s	728.9	14.6 ± 0.6	111 ± 11	3.2 ± 0.2	59.1	6.6 ± 0.3
80 s	716.14	13.3 ± 1.2	182 ± 51	2.3 ± 0.7	50.5	4.4 ± 0.7
200 s	715.15	12.0 ± 0.9	238 ± 106	2.1 ± 0.5	46.5	4.0 ± 0.5
400 s	725.10	12.1 ± 0.8	333 ± 79	2.6 ± 0.7	43.5	3.7 ± 0.6

V_{oc} : Open-circuit voltage; J_{sc} : short-circuit current density; R_s : series resistance; R_{sh} : shunt resistance; FF: fill factor; PCE: power conversion efficiency.

the diffraction peak shift in Sb₂O₃ is more pronounced and the lattice distortion is more significant compared with the counterpart of Sb₂S₃. This can be attributed to the higher surface content of Sb₂O₃ and a higher probability of reaction with Zn. Based on the above analysis, it can be preliminarily determined that after 40 s

of ZnO deposition and subsequent annealing, Zn elements enter both the Sb_2S_3 and Sb_2O_3 lattices in the form of substitutional doping, providing atomic-scale insights into the performance enhancement mechanism.

X-ray photoelectron spectroscopy (XPS) was employed to elucidate the Zn chemical state. Survey scans [Supplementary Figure 5] confirmed elemental presence of C, Sb, S, O, and Zn. High-resolution Sb 3d spectra [Figure 2D] revealed that ZnO deposition reduced Sb_2O_3 content from 79% (control) to 65% (40 s ZnO), consistent with SEM/XRD trends. The S 2p spectrum [Figure 2E] showed typical spin-orbit splitting indicative of S^{2-} in Sb_2S_3 , with a shift to higher binding energies upon ZnO deposition, suggesting reduced sulfur vacancies. Zn 2p peaks [Figure 2F] were absent in the control but faintly detected at 1,022.11 eV and 1,045.50 eV in the 40 s ZnO sample. This chemical shift relative to crystalline ZnO indicates incorporation rather than phase separation. Concurrent shifts in Sb MNN Auger peaks further suggest Zn-S bonding and altered Sb electronic environments.

To probe the depth distribution of Zn doping, XPS depth profiling was performed on the Zn-doping sample (40 s ZnO) versus the control (W/O ZnO) using Ar^+ sputtering at 0.03 nm/s. The Sb 3d_{5/2} binding energy [Figure 2G] decreased with sputtering time, stabilizing beyond 200 s (~6 nm depth). Quantifying the Sb 3d_{5/2} shift relative to the unsputtered surface (Supplementary Figure 6, red spheres) showed an exponential decay ($y = -0.91 + 0.73e^{-x/60}$), with stabilization beyond 200 s (~6 nm depth). This confirms a thin Sb_2O_3 surface layer serving as a hole-blocking but tunnel-permissive oxide. This structure is beneficial for suppressing interfacial recombination while enabling charge extraction. Concurrently, smaller S 2p shifts [Figure 2H and Supplementary Figure 6] and analogous Sb MNN Auger peak displacements (Figure 2I, Supplementary Figure 6, fit: $y = -1.52 + 1.72e^{-x/42}$) indicate Zn_{Sb} substitutional doping confined primarily to the top ~10 nm. Zn_{Sb} substitution was confined to the top ~10 nm, supported by S 2p and Sb MNN trends [Figures 2H and I, Supplementary Figure 6]. This confirms that the ZnO cap limits Sb_2O_3 formation to an ultrathin ~6 nm layer, functioning as a wide-bandgap hole-blocking layer. Then it suppresses interfacial recombination while enabling efficient hole tunneling due to its minimal thickness, consistent with enhanced J_{sc} . Collectively, these depth-resolved analyses demonstrate the dual role of the ZnO interlayer: (1) restricting Sb_2O_3 to nanoscale surface regions, and (2) enabling shallow Zn doping in Sb_2S_3 .

To correlate these interfacial modifications with carrier dynamics, light-intensity-dependent J_{sc} and V_{oc} measurements were conducted [Figure 3]. According to the power-law relationship [Equation 1]^[19], the fitting can obtain the α value.

$$J_{\text{sc}} \propto I^\alpha \quad (1)$$

Where I represents the percentage of irradiation light intensity, and α is the power exponent. As shown in the J_{sc} and irradiation light intensity relationship graph in Figure 3A, yielded $\alpha = 0.90$ (control) versus 0.91 (Zn-doping), indicating marginally improved carrier collection efficiency. More significantly, the function relationship between V_{oc} and light intensity satisfies^[20]:

$$V_{\text{OC}} = \frac{nk_B T}{q} \ln I + C \quad (2)$$

where T , k_B (1.38×10^{-23} J/K), and q (1.60×10^{-19} C) are the Kelvin temperature, Boltzmann constant, and elementary charge, respectively, and n is the ideality factor related to recombination. The diode ideality factor n extracted from decreased from 2.43 (control) to 1.87 (Zn-doping), demonstrating substantial suppression of Shockley-Read-Hall (SRH) recombination via Zn-induced defect passivation. These carrier transport enhancements directly explain the observed performance gains.

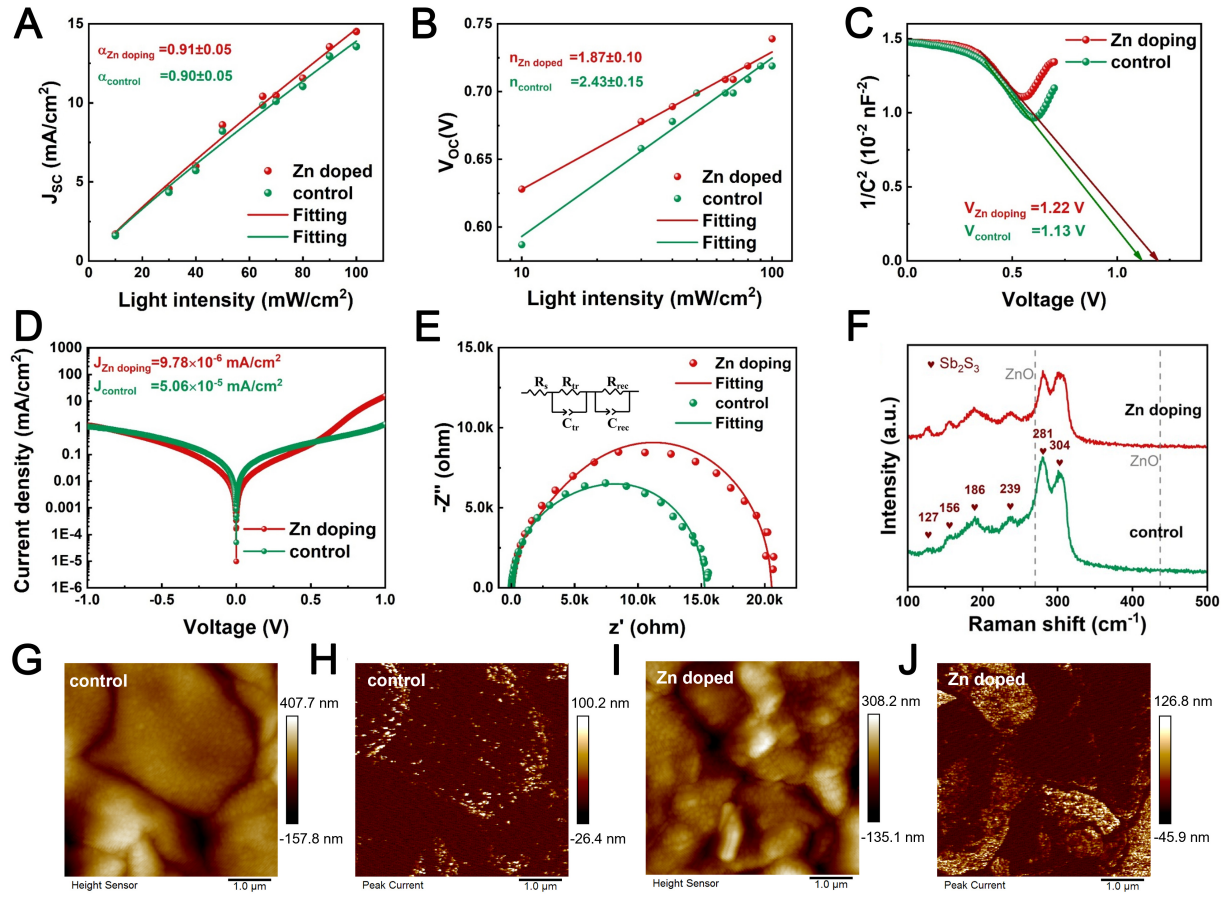


Figure 3. (A) J_{sc} , (B) V_{oc} as a function of light intensity (C) $1/C^2$ - V curves of Sb₂S₃ devices; (D) Dark J - V curves and (E) Nyquist plots of Sb₂S₃ devices; (F) Raman spectra of control and Zn doping Sb₂S₃ thin films; (G and H) AFM images and (I and J) C-AFM images of control and Zn doping Sb₂S₃ thin films. J - V : Density-voltage; V_{oc} : open-circuit voltage; C-AFM: conductive atomic force microscopy; R_s : series resistance; R_{rec} : recombination resistance; J_{sc} : short-circuit current density; C_u and C_{rec} : capacitor.

The C - V characteristics of photovoltaic devices under dark conditions provide critical insights into defect-related properties. We thus measured dark C - V curves at 2 kHz with a 30 mV alternating current (AC) amplitude [Supplementary Figure 7]. By plotting $1/C^2$ versus V [Figure 3C], the built-in potential (V_{bi}) is determined by linearly extrapolating the voltage axis intercept according to [21,22]:

$$\frac{1}{C^2} = \frac{2(V_{bi} - V)}{qS^2\epsilon_0\epsilon_p N_A} \quad (3)$$

Here, C is the capacitance, V is the applied DC bias, S (0.09 cm²) is the cell area, ϵ_0 (8.854×10^{-14} F/cm) is the vacuum permittivity, and ϵ_p (6.67) is the relative permittivity of Sb₂S₃. The control device exhibited a lower V_{bi} (1.13 V) than the Zn-doping counterpart (1.22 V), aligning with the trend in V_{oc} . The hole concentration (N_A) of Sb₂S₃, derived from the slope of the linear fit, increased from 1.32×10^{16} cm⁻³ (control) to 1.47×10^{16} cm⁻³ (Zn-doping). This enhancement is attributed to shallow acceptor states (Zn_{Sb}) induced by P-type doping of Zn, which improves surface conductivity and carrier extraction efficiency, thereby boosting J_{sc} [15].

Dark J - V characteristics further elucidate diode behavior [Figure 3D]. The reverse saturation current (J_0) decreased significantly from 5.06×10^{-5} mA/cm² (control) to 9.78×10^{-6} mA/cm² (Zn-doping), indicating suppressed carrier recombination at the back interface. To gain further insight into the underlying carrier recombination and transport dynamics, we performed EIS measurements under dark conditions and acquired the corresponding Nyquist plots (Figure 3E, inset showing the equivalent circuit). Among them, the

charge transport resistance (R_{tr}) characterizes the carrier collection capability, while the recombination resistance (R_{rec}) is inversely proportional to the carrier recombination rate of the device. Fitted parameters [Supplementary Table 1] revealed that reduced charge transport resistance ($R_{tr} = 3.2 \text{ k}\Omega$ target vs. $5.2 \text{ k}\Omega$ control) confirms enhanced carrier collection, and increased recombination resistance ($R_{rec} = 17 \text{ k}\Omega$ target vs. $10 \text{ k}\Omega$ control), which inversely correlates with recombination rates^[21]. In summary, dark J - V and EIS analyses demonstrate that Zn doping concurrently suppresses carrier recombination and enhances transport/extraction efficiency, directly corroborating the observed performance improvements.

The foregoing analysis demonstrates that Zn doping at the Sb_2S_3 back surface enhances carrier concentration, suppresses recombination, and improves carrier transport efficiency, particularly boosting J_{sc} . To elucidate the underlying physical origins, we systematically investigated the chemical bonding, electronic properties, and energy-level alignments of Zn-doping Sb_2S_3 films. Raman spectroscopy [Figure 3F] revealed no ZnO characteristic peaks (dashed lines in Figure 3F) in either control or Zn-doping films. All observed peaks correspond exclusively to Sb_2S_3 vibrational modes^[23]. The Raman spectrum of Sb_2S_3 arises from four vibrational modes ($2A_1 + 2E$) of its tetrahedral SbS_3 units (C_{3v} symmetry): symmetric stretch ν_s (A_1), asymmetric stretch ν_a (E), symmetric bend δ_s (A_1), and asymmetric bend δ_a (E), with typical intensity ordering $\nu_s > \nu_a$ and $\delta_s > \delta_a$ ^[24]. As shown in Figure 3F, both films exhibit dominant peaks at 281 cm^{-1} [ν_a (Sb-S)] and 304 cm^{-1} [ν_s (Sb-S)], alongside weaker features at 127 cm^{-1} (A_g), 156 cm^{-1} (B_{1g}), 189 cm^{-1} [δ_a (S-Sb-S)], and 239 cm^{-1} [δ_s (S-Sb-S)]. Critically, the intensity ratio I_{304}/I_{281} of symmetric-to-asymmetric stretching vibrations inversely correlates with sulfur vacancy (V_s) concentration. Spectral deconvolution [Supplementary Figure 8A and B] yielded $I_{304}/I_{281} = 1.05$ (control) versus 1.30 (Zn-doping), confirming reduced V_s defects in the Zn-doping film. This reduction is attributed to suppressed Sb_2S_3 volatilization and enhanced crystallinity during ZnO-capped annealing, consistent with diminished non-radiative recombination observed in carrier dynamics.

To further probe the local electrical properties, conductive atomic force microscopy (C-AFM) was performed under dark conditions on both control and Zn-doping Sb_2S_3 films [Figure 3G-J]. Significantly elevated current signals were detected within the large-grained structures of the Zn-doping film compared to the reference. Concurrently, regions passivated by Sb_2O_3 nanobelts at grain boundaries exhibited further suppressed current leakage. These observations collectively demonstrate that enhanced bulk conductivity in Zn-doping Sb_2S_3 directly contributes to higher J_{sc} . While effective defect passivation at grain boundaries via oxygen incorporation, mitigating carrier recombination. These nanoscale electrical characteristics align consistently with the macroscopic device performance enhancements.

To elucidate carrier transport mechanisms, ultraviolet photoelectron spectroscopy (UPS) was performed on control and Zn-doping Sb_2S_3 films. The Fermi level (E_F) and VBM positions were determined by subtracting the secondary electron cutoff edge from the He I excitation source (21.22 eV) [Figures 4A and B]. The control film exhibited $E_F = -3.48 \text{ eV}$ and $\text{VBM} = -6.04 \text{ eV}$, while Zn doping shifted these to $E_F = -3.70 \text{ eV}$ and $\text{VBM} = -5.99 \text{ eV}$. Given the mixed-phase surface composition ($> 80\% \text{ Sb}_2\text{O}_3$), the conduction band minimum (CBM) was referenced to Sb_2O_3 's bandgap. The proposed energy band diagram (Figure 4C, partial data adapted from Ref.^[25]) reveals that the control device possesses high CBM and deep VBM at the back surface form an electron-blocking barrier, which suppresses recombination and transport holes through the oxide tunnel. For Zn-doping device, a 0.22 eV downward shift in E_F and 0.05 eV upward shift in VBM/CBM collectively enhance back-surface field strength. Coupled with the ultrathin oxide layer ($< 10 \text{ nm}$), this configuration promotes hole separation, directly explaining the enhanced V_{oc} and J_{sc} and PCE.

The successful incorporation of Zn and the concomitant suppression of Sb_2O_3 underscore the dual functionality of our ultrathin ZnO layer strategy. This feature distinguishes it from conventional

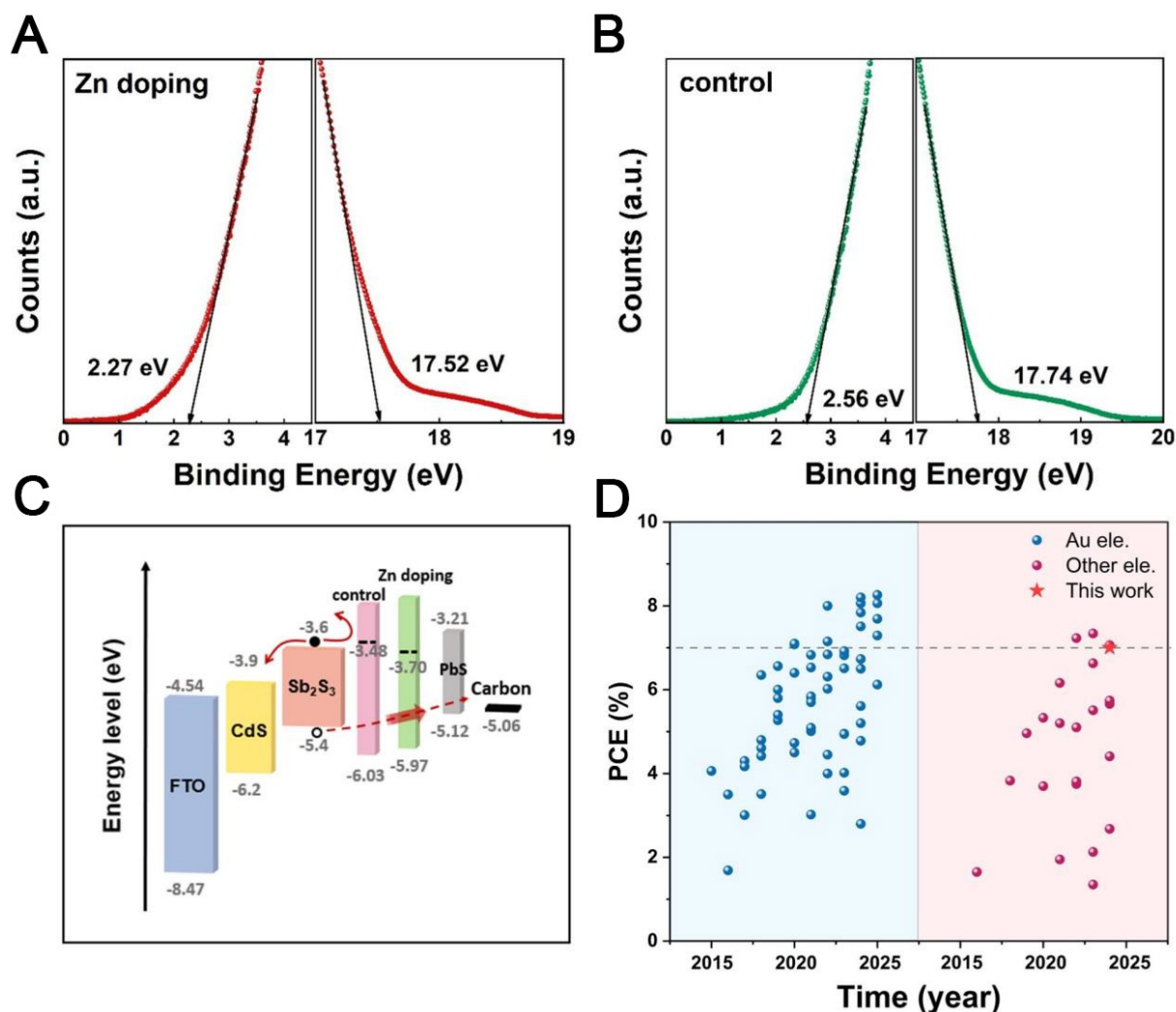


Figure 4. UPS spectrum of (A) control and (B) Zn doping Sb_2S_3 thin films; (C) schematic band diagram and (D) the summarized PCE of previous works of Sb_2S_3 solar cell. UPS: Ultraviolet photoelectron spectroscopy; FTO: fluorine-doped tin oxide; CdS: cadmium sulfide; PCE: power conversion efficiency.

single-function strategies. For instance, prior approaches to alleviate back-contact issues often relied on introducing distinct metal oxide buffer layers (e.g., WO_{3-x} , MoO_2) primarily for hole transport or energy level alignment^[13,17], or focused solely on elemental doping (e.g., solution-processed Zn doping) to tailor electrical properties^[16]. While effective, these strategies typically address only one aspect of the complex interfacial challenges in Sb_2S_3 -based devices. Our approach uniquely integrates a diffusion barrier and a dopant source into a single sub-nanometer-scale layer, simultaneously tackling phase purity, defect passivation, and energy level modulation. This synergistic effect is evidenced by the concurrent improvement in N_A , R_{rec} , and V_{oc} .

Through the strategic implementation of a ZnO protective layer, we optimized both the Sb_2O_3 thickness and achieved surface Zn-doping in Sb_2S_3 , culminating in a 7.00%-efficient, fully inorganic carbon-electrode-based Sb_2S_3 solar cell with an FTO/CdS/ Sb_2S_3 /PbS/Carbon/Ag architecture. Statistically compiled literature data [Figure 4D] position this efficiency at the state-of-the-art performance tier for planar Sb_2S_3 thin-film devices {Surpassing the 7% benchmark indicated by the gray dashed line, and the references are presented in

[Supplementary Materials](#) [1-90]]. Notably, previously reported high-efficiency Sb_2S_3 devices predominantly employ unstable organic hole-transport layers (e.g., Spiro-OMeTAD or P3HT) and cost-prohibitive Au electrodes, fundamentally limiting their practical viability. In contrast, our approach leverages ambient air-annealing and low-cost carbon electrodes to construct an all-inorganic device, which exhibits the competitive efficiency approaching the current Sb_2S_3 record. Based on the enhanced operational stability from inorganic constituents and scalable manufacturability via solution-processable components^[26], this work establishes a transformative pathway toward economically viable, high-performance thin-film solar cells.

CONCLUSION

In this work, we aimed to address the critical challenges of sulfur volatilization and detrimental Sb_2O_3 formation at the back interface of Sb_2S_3 solar cells during high-temperature annealing. By introducing an ultrathin ZnO protective layer, we developed a dual-functional strategy that simultaneously achieves controlled oxygen passivation and effective Zn doping. This synergistic modification suppresses interfacial recombination, optimizes energy level alignment, and enhances carrier transport. Ultimately, in comparison with unmodified devices, the ZnO-modified solar cells exhibit a 17% enhancement in J_{sc} and a significant improvement in PCE, culminating in a state-of-the-art PCE of 7.00% for fully inorganic, carbon-based architectures. This scalable and air-processable strategy provides a promising route toward high-performance, stable, and low-cost Sb_2S_3 solar cells.

DECLARATIONS

Authors' contributions

Idea conception: Chen, G. L.

Writing - original draft: Xia, Y. S.

Writing - editing: Chen, S.; Huang, Z. P.; Li, H.; Lin, L. M.; Xia, Y. S.

Materials characterization: Zhang, J. C.; Cai, J. R.; Huang, G.; Xia, Y. S.

Samples synthesis: Huang, J.; Liu, L. J.; Chen, S.; Xia, Y. S.

Funding acquisition, supervision: Chen, G. L.

All authors participated in the data analysis and result discussions and commented on the manuscript.

Availability of data and materials

The data that support the findings of this study are available from the corresponding author upon reasonable request.

AI and AI-assisted tools statement

Not applicable.

Financial support and sponsorship

This work was supported by the National Natural Science Foundation of China (Grant Nos. 62475044; 62204041), Natural Science Foundation of Fujian Province (Grant Nos. 2025J010031; 2025H6009; 2023I0012).

Conflicts of interest

All authors declared that there are no conflicts of interest.

Ethical approval and consent to participate

Not applicable.

Consent for publication

Not applicable.

Copyright

© The Author(s) 2026.

Supplementary Materials

Supplementary Materials

REFERENCES

- Zheng, J.; Liu, C.; Zhang, L.; et al. Enhanced hydrothermal heterogeneous deposition with surfactant additives for efficient Sb_2S_3 solar cells. *Chem. Eng. J.* **2022**, *446*, 136474. DOI
- Liu, C.; Gong, A.; Zuo, C.; et al. Heterojunction lithiation engineering and diffusion-induced defect passivation for highly efficient $\text{Sb}_2(\text{S,Se})_3$ solar cells. *Energy. Environ. Sci.* **2024**, *17*, 8402-12. DOI
- Ghosh, C.; Varma, B. Optical properties of amorphous and crystalline Sb_2S_3 thin films. *Thin. Solid. Films.* **1979**, *60*, 61-5. DOI
- Kondrotas, R.; Chen, C.; Tang, J. Sb_2S_3 solar cells. *Joule* **2018**, *2*, 857-78. DOI
- Zhao, R.; Yang, X.; Shi, H.; Du, M. Intrinsic and complex defect engineering of quasi-one-dimensional ribbons Sb_2S_3 for photovoltaics performance. *Phys. Rev. Mater.* **2021**, *5*, 054605. DOI
- Wang, S.; Zhao, Y.; Che, B.; et al. A novel multi-sulfur source collaborative chemical bath deposition technology enables 8%-efficiency Sb_2S_3 planar solar cells. *Adv. Mater.* **2022**, *34*, 2206242. DOI
- Li, Y.; Li, R.; Jia, Z.; et al. Precursor engineering of solution-processed Sb_2S_3 solar cells. *Small* **2024**, *20*, 2308895. DOI
- Shen, G.; Ke, A.; Chen, S.; et al. Strong chelating additive and modified electron transport layer for 8.26%-efficient Sb_2S_3 solar Cells. *Adv. Energy. Mater.* **2025**, *15*, 2406051. DOI
- Shockley, W.; Queisser, H. J. Detailed balance limit of efficiency of p - n junction solar cells. *J. Appl. Phys.* **1961**, *32*, 510-9. DOI
- Yao, L.; Lin, L.; Huang, Z.; et al. A liquid medium annealing strategy for highly [041]/[141]-oriented planar antimony sulfide solar cells with 7.23% efficiency. *Nano. Energy.* **2023**, *106*, 108064. DOI
- Chen, C.; Zhao, Y.; Lu, S.; et al. Accelerated optimization of $\text{TiO}_2/\text{Sb}_2\text{Se}_3$ thin film solar cells by high-throughput combinatorial approach. *Adv. Energy. Mater.* **2017**, *7*, 1700866. DOI
- Heo, J. H.; Im, K.; Lee, H. J.; Kim, J.; Im, S. H. Ni,Ti-co-doped MoO_3 nanoparticles with high stability and improved conductivity for hole transporting material in planar metal halide perovskite solar cells. *J. Ind. Eng. Chem.* **2021**, *94*, 376-83. DOI
- Liu, C.; Shen, K.; Lin, D.; et al. Back contact interfacial modification in highly-efficient all-inorganic planar n-i-p Sb_2Se_3 Solar Cells. *ACS. Appl. Mater. Interfaces.* **2020**, *12*, 38397-405. DOI
- Cai, Z.; Dai, C.; Chen, S. Intrinsic defect limit to the electrical conductivity and a two-step p-type doping strategy for overcoming the efficiency bottleneck of Sb_2S_3 -based solar cells. *Solar. RRL.* **2019**, *4*, 1900503. DOI
- Cai, Z.; Chen, S. Extrinsic dopants in quasi-one-dimensional photovoltaic semiconductor Sb_2S_3 : a first-principles study. *J. Appl. Phys.* **2020**, *127*, 183101. DOI
- Tang, R.; Wang, X.; Jiang, C.; et al. n-type doping of Sb_2S_3 light-harvesting films enabling high-efficiency planar heterojunction solar cells. *ACS. Appl. Mater. Interfaces.* **2018**, *10*, 30314-21. DOI
- Chen, S.; Li, M.; Zhu, Y.; et al. A codoping strategy for efficient planar heterojunction Sb_2S_3 solar cells. *Adv. Energy. Mater.* **2022**, *12*, 2202897. DOI
- Chen, S.; Zhao, X.; Shen, G.; et al. All-inorganic Sb_2S_3 -based two-terminal tandem solar cells enable over 10.9% efficiency employing a concise interconnection layer. *J. Mater. Chem. A.* **2024**, *12*, 18148-56. DOI
- Wang, X.; Tang, R.; Jiang, C.; et al. Manipulating the electrical properties of $\text{Sb}_2(\text{S,Se})_3$ film for high-efficiency solar cell. *Adv. Energy. Mater.* **2020**, *10*, 2002341. DOI
- Jiang, C.; Zhou, J.; Tang, R.; et al. 9.7%-efficient $\text{Sb}_2(\text{S,Se})_3$ solar cells with a dithieno [3,2-*b*: 2',3'-*d*] pyrrole-cored hole transporting material. *Energy. Environ. Sci.* **2021**, *14*, 359-64. DOI
- Yin, Y.; Wu, C.; Tang, R.; et al. Composition engineering of Sb_2S_3 film enabling high performance solar cells. *Sci. Bull.* **2019**, *64*, 136-41. DOI
- Heath, J. T.; Cohen, J. D.; Shafarman, W. N. Bulk and metastable defects in $\text{CuIn}_{1-x}\text{Ga}_x\text{Se}_2$ thin films using drive-level capacitance profiling. *J. Appl. Phys.* **2004**, *95*, 1000-10. DOI
- Lin, L.; Liu, J.; Lv, J.; et al. Correlation between native defects and morphological, structural and optical properties of ZnO nanostructures. *J. Alloys. Compd.* **2017**, *695*, 1523-7. DOI
- Hajdeu-Chicarosh, E.; Rotaru, V.; Levchenko, S.; et al. Raman scattering and spectroscopic ellipsometry studies of Sb_2S_3 and Sb_2Se_3 bulk polycrystals. *Phys. Chem. Chem. Phys.* **2023**, *25*, 31188-93. DOI

-
25. Wu, F.; Zhao, Y.; Yao, L.; et al. Manipulating back contact enables over 8%-efficient carbon-based $\text{Sb}_2(\text{S,Se})_3$ solar cells. *Chem. Eng. J.* **2022**, *440*, 135872. DOI
 26. Li, H.; Lin, H.; Liao, X.; et al. 9% certified efficiency record for carbon-based $\text{Sb}_2(\text{S,Se})_3$ solar cells enabled by gradient-oxidized treatment of CdS electron transport layer. *Adv. Funct. Mater.* **2025**, *36*, e20949. DOI

Disclaimer/Publisher's Note: All statements, opinions, and data contained in this publication are solely those of the individual author(s) and contributor(s) and do not necessarily reflect those of OAE and/or the editor(s). OAE and/or the editor(s) disclaim any responsibility for harm to persons or property resulting from the use of any ideas, methods, instructions, or products mentioned in the content.



© The Author(s) 2026. Open Access This article is licensed under a Creative Commons Attribution 4.0 International License (<https://creativecommons.org/licenses/by/4.0/>), which permits unrestricted use, sharing, adaptation, distribution and reproduction in any medium or format, for any purpose, even commercially, as long as you give appropriate credit to the original author(s) and the source, provide a link to the Creative Commons license, and indicate if changes were made.